

A Computational Framework for Characterizing Viscoelastic Effects Surrounding a Buried Magma Reservoir

C. Rucker^{1*}, B. Lee³, J. Gopalakrishnan³, B.A. Erickson^{1,2}, and L. Karlstrom²

¹Department of Computer and Information Science, University of Oregon,
Eugene, OR, USA

²Department of Earth Sciences, University of Oregon,
Eugene, OR, USA

³Department of Mathematics and Statistics, Portland State University,
Portland, OR, USA

Email: *crucker@uoregon.edu

Abstract—We present a numerical framework for modeling the temporal evolution of ground deformation caused by a subsurface, pressurized magma reservoir situated within a viscoelastic medium. The host rock surrounding an oblate, ellipsoidal magma reservoir behaves as a Maxwell material. Temporal evolution due to the viscous effects are encoded as source terms on the static equilibrium equations; the coupled system is solved via high-order FEM and explicit time-stepping. We derive numerically stable time steps and verify convergence at the theoretical rate. For an applied, sinusoidal pressure at the reservoir boundary, the model is shown to reproduce the theoretical relationship between stress and strain for Maxwell materials.

I. Introduction and Literature Review

Understanding the temporal frequency of volcanic eruptions is a long-standing and important scientific problem. As magma is transported from the Earth’s mantle into the upper crust, magmatic reservoirs are coupled to surrounding deformations the dynamics of which influence volcanic unrest. In the vicinity of a long-lived magma reservoir, extreme temperature profiles may heat the surrounding host rock sufficiently so that the rock may no longer have a purely elastic response. Various models have been proposed for simulating magma reservoir behavior; many of these models focus on answering two key questions:

- 1) Given a deformation profile at the Earth’s surface, can we determine the geometry, depth, and pressure of the associated magma reservoir?
- 2) What are the conditions that cause a subsurface magma reservoir to erupt?

Early models assume a perfectly-elastic rheology of the host rock [1][2]. These elastic models have been widely used to interpret geodetic data gathered from various volcanic sites [1] [2][3]. However, [3] observed that in order to reproduce the observed uplift measured at Pozzuoli, an unreasonable overpressure was required at the reservoir boundary. In the formation of a magma reservoir, if the timescale over which the chamber evolves due to

mass injection is lower than the heat diffusion timescale, a ductile region surrounding the reservoir may evolve as crustal material is heated beyond the brittle-ductile transition temperature [4].

More recent models assume that the host rock behaves viscoelastically [5][6][7][8]. These models allow for a viscous component in the medium. Though initially constrained by constant coefficient viscosity, the development of a model using a viscoelastic shell around the reservoir allowed for simulation of a ductile region situated within a perfectly-elastic crust [9]. In [5], it was found that when viscosity was allowed to vary as a function of space (dependent on a background temperature profile), that the viscoelastic model could reproduce the same displacements as the elastic model but with more reasonable overpressures along the reservoir boundary. However, these overpressures still seemed to be fairly large and unreasonable [5].

Though the viscoelastic model seems to be a better choice for modeling ground deformations, it might not be much better at predicting eruptions. A condition for the onset of an eruption is that the reservoir walls fail. This failure indicates the initiation of a dike to transport magma throughout the host rock and possibly to the surface. The magma overpressure that the walls of a chamber can sustain before failing depend on the rheology of the host rock[7]. In fact, for brittle failure, the overpressure at failure onset is independent of the host rock viscosity [10]. Thus, it may be important to consider the effect that the temperature profile surrounding a magma reservoir has on the elastic material parameters of the medium. Young’s modulus plays an important role in the speed at which a dike can propagate as well as the dike’s thickness [11]. Ultimately this means that the rate at which magma can be transported out of the reservoir is dependent on Young’s modulus within the host rock.

In this paper, we present a robust numerical framework for simulating the thermo-mechanical behavior of a subsurface magma reservoir in an isotropic, heterogeneous, viscoelastic space. Our model uses spatially dependent material properties derived from a steady temperature distribution within the medium. Both viscous and elastic material parameters are considered to be affected by temperature. After detailing the numerical framework we verify accuracy using a manufactured solution. Finally we use our framework to characterize the system's response to non-constant, viscoelastic material properties.

II. Problem Formulation

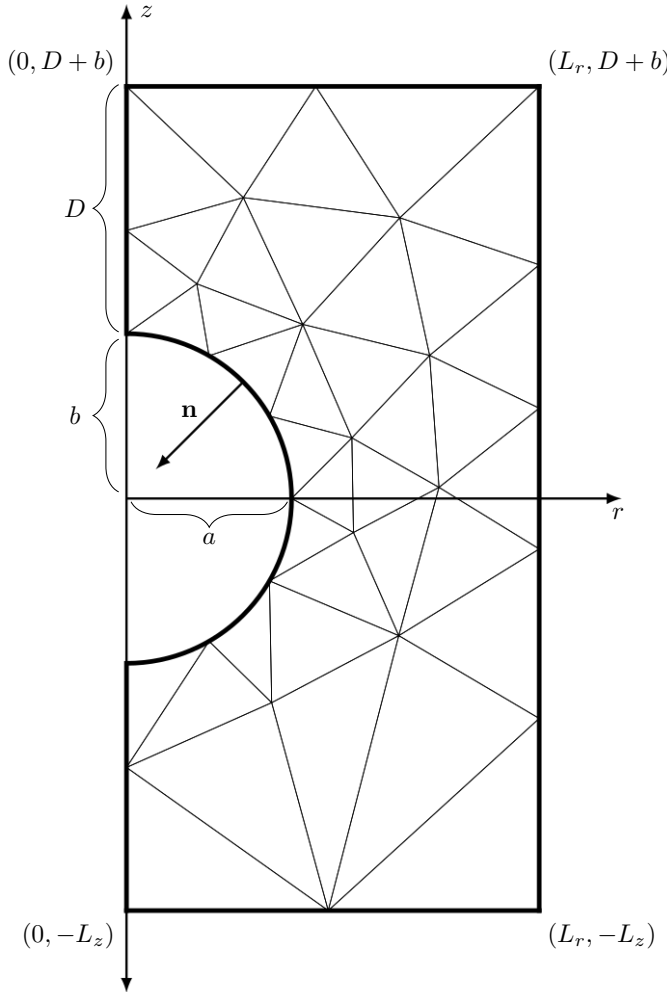


Fig. 1: The region outside a subsurface, ellipsoidal magma reservoir. The reservoir has a horizontal axis $a > 0$ and vertical axis $b > 0$. The distance from the top of the reservoir to the surface is $D > 0$. The region is bounded by a maximal depth L_z and maximal distance from the radial center L_r .

A. Description

We simulate a subsurface magma reservoir in an isotropic, viscoelastic half-space. The reservoir is assumed to evolve in time as a steady supply of molten material is

provided from within the Earth's mantle. There are two primary interactions to consider:

- As mass is injected into the reservoir, how does the the pressure along the reservoir boundary evolve?
- Given a pressure along the reservoir wall, how does the surrounding crust of the Earth deform?

Our approach is to consider two systems, one internal to the cavity and the other external, which are coupled along the reservoir boundary interface. In developing our framework, we focus on the external system dynamics while drawing insight from the internal system.

B. Internal System

With regards to the reservoir, let V_c, P_c, ρ_c, T_c denote volume, pressure, density, and temperature, respectively. We consider the reservoir to be a spatially-uniform system which is governed by the mass balance

$$\rho_c \frac{dV_c}{dt} + V_c \frac{d\rho_c}{dt} = \dot{M}_{\text{in}} - \dot{M}_{\text{out}}, \quad (1)$$

and $\dot{M}_{\text{in}}, \dot{M}_{\text{out}}$ denote the mass flow rates in and out of the system. Density is determined by a linear equation of state

$$\rho_c = \rho_0 \left(1 + \frac{P_c}{\kappa}\right) \quad (2)$$

where ρ_0 is a reference density and κ is a constant bulk compressibility. This allows us to make explicit the dependence of Equation 1 on pressure

$$\rho_c \frac{dV_c}{dt} + \frac{\rho_0 V_c}{\kappa} \frac{dP_c}{dt} = \dot{M}_{\text{in}} - \dot{M}_{\text{out}}. \quad (3)$$

We supplement Eq. Equation 3 with an initial pressure and reservoir volume

$$P_c(t = 0) = P_0, \quad (4a)$$

$$V_c(t = 0) = V_0. \quad (4b)$$

Solutions to Equation 3 dictate the appropriate pressure data to impose at the reservoir boundary so long as the rate of change for volume is known. Computing an approximation to the change in the reservoir volume requires knowledge about the displacement field in the external system.

C. External System

1) Domain Geometry: We employ a cylindrical coordinate system (r, z, θ) with an origin at the cavity's center. As shown in Fig. Figure 1, the cavity is assumed to be ellipsoidal with horizontal axis $a > 0$ and vertical axis $b > 0$ with its center at depth $D + b$. Maximum depth of the domain is denoted by L_z and the maximum distance from the center of radial symmetry is denoted by L_r . We reduce the problem by an axisymmetric assumption to avoid the computational cost of 3-D problems. This assumption of axisymmetry means the problem shows no

variation along the θ -coordinate enabling solutions in the (r, z) -plane.

We construct the region outside of the cavity by intersecting a closed, rectangular region $\mathcal{D} = \{(r, z) \in \mathbb{R}^2 \mid 0 \leq r \leq L_r, -L_z \leq z \leq D + b\}$ and a punctured domain $\mathcal{B} = \{(r, z) \in \mathbb{R}^2 \mid \frac{r^2}{a^2} + \frac{z^2}{b^2} \geq 1\}$. The region Ω outside of the cavity is defined by

$$\Omega = \mathcal{D} \cap \mathcal{B}.$$

2) Governing Equations: For computational efficiency, we employ a quasi-dynamic model for elastodynamics. Our particular approach assumes the medium is a Maxwell material and, at each point in time, uses a Maxwell aging law to determine sourcing data for the equations of static equilibrium. Let $\mathbf{u}, \underline{\boldsymbol{\varepsilon}}, \underline{\boldsymbol{\gamma}}, \underline{\boldsymbol{\sigma}}$ be, respectively, the displacement vector, the total strain tensor, the viscous strain tensor, and the stress tensor. Displacements in the Earth are related to strains by

$$\underline{\boldsymbol{\varepsilon}}(\mathbf{u}) = \varepsilon_{ij}(\mathbf{u}) = \frac{1}{2} \left(\frac{\partial u_i}{\partial x_j} + \frac{\partial u_j}{\partial x_i} \right) \quad (5)$$

for $i, j \in \{r, z, \theta\}$. The relevant governing equations are:

$$\text{div } \underline{\boldsymbol{\sigma}} = \mathbf{f}, \quad (6a)$$

$$\dot{\underline{\boldsymbol{\gamma}}} = \mathbf{A} \underline{\boldsymbol{\sigma}}, \quad (6b)$$

$$\underline{\boldsymbol{\sigma}} = \mathbf{E}(\underline{\boldsymbol{\varepsilon}} - \underline{\boldsymbol{\gamma}}), \quad (6c)$$

where \mathbf{E} is the 4th-order elastic stiffness tensor defined for any rank-2 tensor $\underline{\boldsymbol{\varphi}}$ as

$$\mathbf{E} \underline{\boldsymbol{\varphi}} = 2\mu \underline{\boldsymbol{\varphi}}_{ij} + \lambda \varphi_{kk} \delta_{ij}, \quad (7)$$

with Lamé parameters μ and λ while \mathbf{A} is the 4th-order viscous compliance tensor defined by

$$\mathbf{A} \underline{\boldsymbol{\varphi}} = \frac{1}{2\eta} (\varphi_{ij} - \frac{1}{3} \varphi_{kk} \delta_{ij}), \quad (8)$$

for viscosity η . Equation 6a is static equilibrium. Equation 6b is the aging law for a Maxwell material and Equation 6c is Hooke's Law. Boundary conditions are imposed by partitioning the boundary $\partial\Omega$ of Ω . We let $\Gamma_{\text{kinematic}} \subseteq \partial\Omega$ and $\Gamma_{\text{traction}} = \partial\Omega \setminus \Gamma_{\text{kinematic}}$, and impose

$$\mathbf{u} = \mathbf{g} \quad \text{on } \Gamma_{\text{kinematic}}, \quad (9a)$$

$$\underline{\boldsymbol{\sigma}} \mathbf{n} = -\mathbf{P} \quad \text{on } \Gamma_{\text{traction}}, \quad (9b)$$

where \mathbf{n} is the outward unit normal to the domain Ω . In addition to boundary conditions, we must also supplement the aging law Equation 6b with initial condition

$$\underline{\boldsymbol{\gamma}}(r, z, t = 0) = \underline{\boldsymbol{\gamma}}_0(r, z). \quad (10)$$

III. Numerical Methods

Here we provide the numerical components which make up our framework. We pair a finite difference discretization in time with a finite element method in space. At each time step, the spatial problem is governed

by static equilibrium with a time-dependent source term. This source term is determined by our Maxwell aging law Equation 6b and accounts for viscous effects within the system. Simulations are done using Python code developed on top of the free and open source multi-physics library NGSolve¹ [12][13][14]. This section outlines the static problem, the temporal discretization, and provides a re-scaling of the problem.

A. Static solve

We solve the equilibrium equations Equation 6a subject to boundary conditions Equation 9a, Equation 9b using a finite element method. To properly detail the method we discuss an integration by parts which arises when deriving the weak form of the problem. For the remainder of this paper, we adopt the notation $(\underline{\boldsymbol{\phi}}, \underline{\boldsymbol{\psi}})_r$ to denote the integral over Ω of $r \underline{\boldsymbol{\phi}} \cdot \underline{\boldsymbol{\psi}}$ when $\underline{\boldsymbol{\phi}}$ and $\underline{\boldsymbol{\psi}}$ are vector functions. When $\underline{\boldsymbol{\phi}}, \underline{\boldsymbol{\psi}}$ are matrix functions we take the notation $(\underline{\boldsymbol{\phi}}, \underline{\boldsymbol{\psi}})_r$ to denote the integral over Ω of $r \underline{\boldsymbol{\phi}} : \underline{\boldsymbol{\psi}}$. The inner product of vector functions utilizes the dot product, denoted by “.”, while the inner product of matrix functions uses the Frobenius inner-product, which we denote “:”. To convey the details of our method we consider a rank 2 tensor $\underline{\boldsymbol{\tau}}$ expressed with respect to our (r, z) -coordinates. For such a $\underline{\boldsymbol{\tau}}$, we may express the cylindrical divergence operator by

$$\text{div } \underline{\boldsymbol{\tau}} = \nabla \cdot \underline{\boldsymbol{\tau}} + \frac{1}{r} \begin{bmatrix} \tau_{rr} - \tau_{\theta\theta} \\ \tau_{rz} \end{bmatrix}, \quad (11)$$

where $\nabla \cdot \underline{\boldsymbol{\tau}}$ denotes the usual Cartesian divergence of $\underline{\boldsymbol{\tau}}$. We proceed by considering a test function $\underline{\boldsymbol{\phi}}$ and, in the usual fashion, multiply Equation 11 by $\underline{\boldsymbol{\phi}}$ and integrate over Ω to get

$$(\text{div } \underline{\boldsymbol{\tau}}, \underline{\boldsymbol{\phi}})_r = \langle \underline{\boldsymbol{\tau}}, \underline{\boldsymbol{\phi}} \rangle_r - (\tau_{\theta\theta}, \phi_r) - (\underline{\boldsymbol{\tau}}, \text{grad } \underline{\boldsymbol{\phi}})_r. \quad (12)$$

Furthermore, if $\underline{\boldsymbol{\tau}}$ can be written as the product of the elastic tensor \mathbf{E} and some tensor $\hat{\underline{\boldsymbol{\tau}}}$, then

$$\tau_{ij} = 2\mu \hat{\tau}_{ij} + \lambda \text{Tr}(\hat{\underline{\boldsymbol{\tau}}}) \delta_{ij}, \quad (13)$$

and

$$(\text{div } \underline{\boldsymbol{\tau}}, \underline{\boldsymbol{\phi}})_r = \langle \underline{\boldsymbol{\tau}}, \underline{\boldsymbol{\phi}} \rangle_r - (\underline{\boldsymbol{\tau}}, \underline{\boldsymbol{\varepsilon}}(\underline{\boldsymbol{\phi}}))_r. \quad (14)$$

Now, for any domain $T \subset \mathbb{R}^2$, we will denote by $\mathcal{P}_p(T)$ the space of binomials of degree at most p in \mathbb{R}^2 , restricted to T . Given a triangulation of Ω , denoted by Ω_h , the Lagrange finite element space of order p consists of those functions which are continuous on Ω whose restriction to each element of Ω_h is a polynomial of degree p . We denote the Lagrange finite element space of order p by

$$V_{h,p} = \{v \in C^0(\Omega) : v|_K \in \mathcal{P}_p(K), \text{ for all } K \in \Omega_h\}. \quad (15)$$

¹Source code available at <https://bitbucket.org/jayggg/magmaxism/src/master/>

Solutions to the static problem will be approximate displacements consisting of an r and z component and thus we construct a compound space where each component is an element of $V_{h,p}$, namely,

$$\mathbf{V}_{h,p} = V_{h,p} \times V_{h,p}. \quad (16)$$

We seek an approximate $\mathbf{u}_h \in \mathbf{V}_{h,p}$ such that

$$\begin{aligned} (\mathbf{E}\underline{\underline{\varepsilon}}(\mathbf{u}_h), \underline{\underline{\varepsilon}}(\mathbf{v}))_r &= - (f, \mathbf{v})_r + (\mathbf{E}\underline{\underline{\gamma}}(\mathbf{u}_h), \underline{\underline{\varepsilon}}(\mathbf{v}))_r \\ &+ \langle \mathbf{E}(\underline{\underline{\varepsilon}}(\mathbf{u}_h) - \underline{\underline{\gamma}}(\mathbf{u}_h)), \mathbf{v} \rangle_r \end{aligned} \quad (17)$$

for every $\mathbf{v} \in \mathbf{V}_{h,p}$.

B. Temporal discretization

Rather than explicitly solving Equation 6b we instead consider $\underline{\underline{C}} = \mathbf{E}\underline{\underline{\gamma}}$ and make the appropriate substitution in the governing equations. By multiplying Equation 6b by \mathbf{E} we get a modified aging law

$$\dot{\underline{\underline{C}}} = \frac{\mu}{\eta} \text{dev } \underline{\underline{\sigma}}. \quad (18)$$

Time integration is carried out using the first-order accurate forward Euler method. At each time step, we solve the static system governed by Equation 6a and use the computed displacement to approximate $\underline{\underline{C}}$ at the next time step. The procedure to integrate from time step t^n to time step t^{n+1} over step size Δt is as follows:

- 1) Set boundary conditions

$$\mathbf{u}_h^n = \mathbf{g} \quad \text{on } \Gamma_{\text{kinematic}}, \quad (19)$$

$$\underline{\underline{\sigma}}_h^n \mathbf{n} = -\mathbf{P} \quad \text{on } \Gamma_{\text{traction}}, \quad (20)$$

- 2) solve the static problem by finding \mathbf{u}_h^n such that variational form Equation 17 is satisfied for every test function $\mathbf{v}_h \in \mathbf{V}_{h,p}$.

- 3) Use \mathbf{u}_h^n to update $\underline{\underline{C}}$ by

$$\underline{\underline{C}}^{n+1} = \underline{\underline{C}}^n + \Delta t \mathbf{E} \mathbf{A} (\mathbf{E} \underline{\underline{\varepsilon}}(\mathbf{u}_h^n) - \underline{\underline{C}}^n) \quad (21)$$

C. Non-dimensionalization

In practice, the scales present in the system could introduce large round-off errors as well as an unreasonable computational burden. To mitigate these drawbacks, we eliminate broad ranges in the system's length and time scale via a non-dimensionalization. We begin by handling the scaling of the domain before addressing governing equations. Let $r = a\tilde{r}$, $z = a\tilde{z}$ and $\underline{\underline{\sigma}} = P_0 \tilde{\underline{\underline{\sigma}}}$. $\tilde{\mathcal{D}} = \{(\tilde{r}, \tilde{z}) \in \mathbb{R}^2 \mid 0 \leq \tilde{r} \leq \frac{L_r}{a}, -\frac{L_z}{a} \leq \tilde{z} \leq \frac{D+b}{a}\}$ and $\tilde{\mathcal{B}} = \{(\tilde{r}, \tilde{z}) \in \mathbb{R}^2 \mid \tilde{r}^2 + \frac{a^2}{b^2} \tilde{z}^2 \geq 1\}$ then our resulting scaled domain is given by

$$\tilde{\Omega} = \tilde{\mathcal{D}} \cap \tilde{\mathcal{B}}. \quad (22)$$

Due to our choice to scale both spatial coordinates by the same characteristic scale a and linearity of differential

operators, we get the scaled form of the equilibrium equations Equation 6a is

$$\text{div } \tilde{\underline{\underline{\sigma}}} = \frac{a}{P_0} f, \quad (23)$$

and Hooke's law Equation 6c becomes

$$\tilde{\underline{\underline{\sigma}}} = \frac{1}{P_0} \mathbf{E}(\underline{\underline{\varepsilon}} - \underline{\underline{\gamma}}). \quad (24)$$

For scaling the aging law we consider a time scale $t = \xi \tilde{t}$ as well as the scaling $\underline{\underline{C}} = P_0 \tilde{\underline{\underline{C}}}$ and scale our modified aging law Equation 18 to become

$$\partial_{\tilde{t}} \tilde{\underline{\underline{C}}} = \frac{\xi \mu}{\eta} \text{dev } \tilde{\underline{\underline{\sigma}}}. \quad (25)$$

D. Stability

Owing to the use of an explicit time-stepping scheme, it is necessary to establish conditions for which time stepping is stable. Moreover, it will be useful to characterize this stability condition in terms of the non-dimensional number which scales the right-hand-side of Equation 25. As this non-dimensional quantity is related to the well-known Deborah number, De , we will denote it by

$$\frac{\xi \mu}{\eta} = \frac{1}{De} = De^{-1}. \quad (26)$$

To carry out this analysis we will use the relationship

$$\mathbf{E} \mathbf{A} \underline{\underline{\varphi}} = \frac{\mu}{\eta} \text{dev } \underline{\underline{\varphi}} \quad (27)$$

where $\underline{\underline{\varphi}}$ is any second-rank tensor. Further, express the deviatoric operator as matrix multiplication. That is, let

$$\mathcal{D} = \begin{bmatrix} \frac{2}{3} & -\frac{1}{3} & -\frac{1}{3} & 0 \\ -\frac{1}{3} & \frac{2}{3} & -\frac{1}{3} & 0 \\ -\frac{1}{3} & -\frac{1}{3} & \frac{2}{3} & 0 \\ 0 & 0 & 0 & 1 \end{bmatrix} \quad (28)$$

so that Equation 27 can be written as

$$\mathbf{E} \mathbf{A} \underline{\underline{\varphi}} = \frac{\mu}{\eta} \mathcal{D} \underline{\underline{\varphi}}. \quad (29)$$

Now consider the forward Euler discretization of the aging law, Equation 25, expressing the evolution from time t^n to time t^{n+1}

$$\tilde{\underline{\underline{C}}}^{n+1} = (\mathbf{I} - \Delta t De^{-1} \mathcal{D}) \tilde{\underline{\underline{C}}}^n + \Delta t De^{-1} \mathcal{D} \mathbf{E} \underline{\underline{\varepsilon}}^n. \quad (30)$$

Stability of the time stepping scheme is then dependent on the eigenvalues of the growth-factor matrix $\mathbf{I} - \Delta t De^{-1} \mathcal{D}$ and whether we can bound its spectral radius using an appropriate choice for Δt . Eigenvalues for the growth-factor matrix are

$$\lambda_1 = 1, \quad (31a)$$

$$\lambda_2 = 1 - \frac{2}{3} \Delta t De^{-1}, \quad (31b)$$

$$\lambda_3 = 1 - \Delta t De^{-1}, \quad (31c)$$

where λ_3 appears as a repeated eigenvalue. The choice of Δt will only influence λ_2 , and λ_3 . From Equation 31b the condition on Δt is that $\Delta t < 3De$ but Equation 31c gives the condition $\Delta t < 2De$. Thus for the sake of stability, the time step Δt should be smaller than $2De$.

Additionally, the time step must be sufficiently small to resolve contributions from time-dependent boundary data. Let δt be the largest time step resolving time-dependent data on each of the domain boundaries. A sufficient time step is then chosen by

$$\Delta t < \min\{2De, \delta t\}. \quad (32)$$

E. Verification

We verify accuracy of our numerical method using the method of manufactured solutions [15]. This verification technique lets us choose arbitrary solution fields $u^*(r, z, t), C^*(r, z, t)$ to act as exact solutions necessary for measuring convergence. u^* and C^* need not satisfy the governing equations or boundary conditions. We treat this issue by appending corrective terms to those conditions which the manufactured solutions do not satisfy. This process is shown in detail later in this section. We base our manufactured solution off of the well known solution to the pressurize magma cavity problem in an elastic half-space [16] given by

$$\mathbf{u}_e = \frac{P_0 a^3}{4\mu(r^2 + z^2)^{3/2}} \begin{bmatrix} r \\ z \end{bmatrix}. \quad (33)$$

Define the manufactured solutions u^*, C^* by

$$u^*(r, z, t) = (2 - e^{-t})\mathbf{u}_e, \quad (34)$$

$$C^*(r, z, t) = (1 - e^{-t})\mathbf{E}\underline{\underline{\epsilon}}(\mathbf{u}_e). \quad (35)$$

This choice of u^* and C^* satisfies the equilibrium equations but not the aging law. The discrepancy caused by a manufactured solution which does not satisfy the aging law is accounted for by appending a corrective term and solving

$$\dot{\underline{\underline{C}}} = \mathbf{E}\mathbf{A}\underline{\underline{\sigma}} + \mathbf{G} \quad (36)$$

where \mathbf{G} is determined from the manufactured solutions to be

$$\mathbf{G} = e^{-t}\sigma^* - \frac{\mu}{\eta} \text{dev } \sigma^*. \quad (37)$$

σ^* is regarded as the manufactured stress and can be obtained by computing

$$\sigma^* = \mathbf{E}\underline{\underline{\epsilon}}(\mathbf{u}_e). \quad (38)$$

Figure 2 shows the rate of convergence in the measured spatial error over successive mesh refinements when polynomials of degree 3 are used as a basis for the finite element space. This agrees with FEM theory which predicts a convergence rate of $p + 1$ when polynomials of degree p are used and error is measured with respect to the L^2 norm [17]. The same convergence pattern is observed for

h	$\ c - c_h\ $	c -rate	$\ \mathbf{u} - \mathbf{u}_h\ $	\mathbf{u} -rate
$h/2$	5.25×10^{-9}		1.84×10^{-8}	
$h/4$	7.17×10^{-10}	2.87	1.31×10^{-9}	3.81
$h/8$	9.13×10^{-11}	2.97	8.41×10^{-11}	3.96
$h/16$	1.14×10^{-11}	3.00	5.24×10^{-12}	4.00

Fig. 2: Spatial convergence data, measured with respect to the L^2 -norm, for a single time step of $\Delta t = 10e^{-7}$ using polynomials of degree 3.

Δt	$\ c - c_h\ $	c -rate	$\ \mathbf{u} - \mathbf{u}_h\ $	\mathbf{u} -rate
$\Delta t/2$	1.75×10^{-1}		1.18×10^{-6}	
$\Delta t/4$	8.85×10^{-2}	0.99	5.96×10^{-7}	0.99
$\Delta t/8$	4.46×10^{-2}	0.99	3.01×10^{-7}	0.99

Fig. 3: Temporal convergence data measured at point $(\tilde{A}, 0)$ under the discrete ℓ^2 -norm.

polynomials with degree greater than 3 but the L^2 -error drops below machine precision leading to round-off error in the rate computation.

To measure convergence in the temporal domain we select a single point in space and perform successive mesh refinements in time. Figure 3 shows that both $\underline{\underline{C}}$ and \mathbf{u} exhibit rate-1 convergence. Considering the first-order accurate forward Euler method is used to approximate $\underline{\underline{C}}$ this verifies proper accuracy is attained in computing $\underline{\underline{C}}$.

F. Phase lag analysis

To discern the quality of our method, we survey some expected patterns concerning the link between the viscosity of the regime and the phase lag phenomenon that results between stress and strain. The expectation is that the viscous component of strain will put stress and elastic strain out of phase. (It should be the case that stress and elastic strain are in phase, so only viscous components will contribute to phase lag.) Although our problem considers a tensor form of Hooke's law, we have also assumed in our simulations an isotropic homogeneous material with (in particular) constant viscosity. As such, it suffices to consider the Maxwell model in one dimension. In this case, the stress σ and strain ϵ are related by the constitutive law

$$\dot{\epsilon} = \frac{1}{\mu}\dot{\sigma} + \frac{1}{\eta}\sigma \quad (39)$$

which we transform into Fourier space by making the ansatz

$$\epsilon(t) = e^{i\omega t}\hat{\epsilon}(\omega); \quad \sigma(t) = e^{i\omega t}\hat{\sigma}(\omega)$$

after which substituting into the 1D constitutive law yields

$$\dot{\epsilon}(t) = i\omega e^{i\omega t}\hat{\epsilon}(\omega) = \left(\frac{1}{\mu}i\omega + \frac{1}{\eta}\right)e^{i\omega t}\hat{\sigma}(\omega). \quad (40)$$

Dividing the above by $i\omega e^{i\omega t}$ yields

$$\hat{\epsilon}(\omega) = \hat{\mu}(\omega)\hat{\sigma}(\omega) \quad (41)$$

or more usefully,

$$\hat{\sigma}(\omega) = \frac{1}{\hat{\mu}(\omega)} \hat{\varepsilon}(\omega) =: \hat{\gamma}(\omega) \hat{\varepsilon}(\omega) \quad (42)$$

The storage and loss moduli, $\hat{\mu}_1, \hat{\mu}_2$, are determined to be

$$\hat{\mu}_1 = \frac{\eta^2 \omega^2 \mu}{\eta^2 \omega^2 + \mu^2} \quad (43)$$

$$\hat{\mu}_2 = \frac{\eta \omega \mu^2}{\eta^2 \omega^2 + \mu^2}. \quad (44)$$

We compute real and imaginary parts of $\hat{\gamma}$ as

$$\hat{\gamma}_1 = \frac{\hat{\mu}_1}{|\hat{\mu}|^2}; \quad \hat{\gamma}_2 = -\frac{\hat{\mu}_2}{|\hat{\mu}|^2}. \quad (45)$$

In our simulations, we impose a sinusoidal stress $\sigma(t) = \sin(\omega t)$ on the boundary. We will arrive at a result for phase lag measurement independent of amplitude on this stress. We mirror integral manipulations done to the convolution relationship in [18] equation (1.2.32b) of chapter 1,

$$\varepsilon(t) = [\gamma * \sigma](t).$$

We find

$$\varepsilon(t) = \hat{\gamma}_2(\omega) \cos \omega t + \hat{\gamma}_1(\omega) \sin \omega t \quad (46)$$

from which we measure phase lag by

$$\tan \phi = \frac{\hat{\gamma}_2(\omega)}{\hat{\gamma}_1(\omega)}$$

where we recognize $\hat{\gamma}_1$ and $\hat{\gamma}_2$ as analogues to storage and loss moduli but instead with regards to measuring phase lag of strain given stress.

Assembling all of the above gives phase lag

$$\phi = \arctan \frac{\hat{\gamma}_2}{\hat{\gamma}_1} = \arctan \left(-\frac{\hat{\mu}_2}{\hat{\mu}_1} \right) = -\arctan \frac{1}{\text{De}}$$

De is the Deborah number

$$\text{De} = \frac{\eta \omega}{\mu}$$

where η is our constant viscosity and μ is Lamé's first parameter.

Our numerical computation of phase lag is conducted by discerning when stress attains a local minimum and measuring the amount of time it takes for strain to respond accordingly. In particular, what we measure is the normal component of traction $\underline{\sigma} \mathbf{n} \cdot \mathbf{n}$ compared to its analogous normal counterpart in strain $\underline{\varepsilon} \mathbf{n} \cdot \mathbf{n}$ at a specific point on the chamber wall. Which point is immaterial, so long as the computation is conducted on the chamber wall, where expected traction is known precisely.

IV. Conclusion

A rigorous framework is presented to investigate the evolution of crustal displacements due to a pressurized, subsurface magma reservoir. We derive conditions on the time step, which guarantees stability of the aging law, and show that the numerical solution converges to the exact solution at the theoretical rate of convergence. Additionally, the model is shown to reproduce a

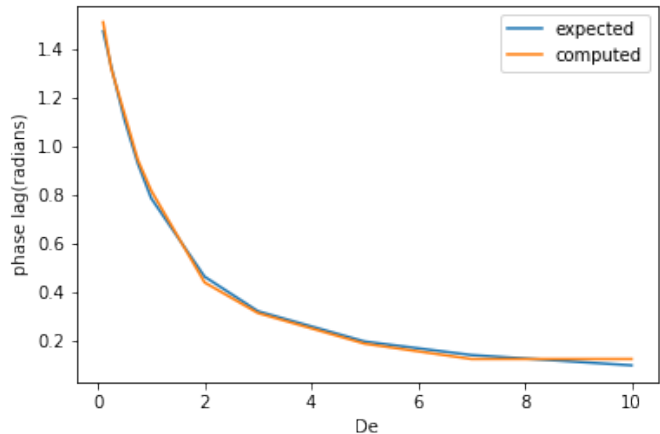


Fig. 4: Comparison of the phase lag between stress and strain. The expected curve represents the theoretical phase lag and the computed curve represents the phase lag observed from numerical results.

characteristic phase lag, between applied stress and resulting strain, which is intrinsic to viscoelastic systems.

This Directed Research Project(DRP) is part of an ongoing collaboration effort to construct a rigorous, transparent, and accessible model for volcano rupture dynamics. Presently, we are working on extending the framework proposed in this DRP to account for temperature-dependent rheological parameters. This extension is motivated by the influence that the thermal state of the Earth's crust has on the temporal evolution of the deformation field [5].

The current model relies on user-supplemented boundary conditions, however, knowing the correct conditions to impose is a difficult task. For this reason, expanding the current framework to infer pressure conditions from solving a mass balance internal to the reservoir could allow for more realistic pressures along the reservoir boundary.

References

- [1] M. Kiyoo, "Relations between the eruptions of various volcanoes and the deformations of the ground surfaces around them," *Earthq Res Inst*, vol. 36, pp. 99–134, 1958.
- [2] D. McTigue, "Elastic stress and deformation near a finite spherical magma body: resolution of the point source paradox," *Journal of Geophysical Research: Solid Earth*, vol. 92, no. B12, pp. 12931–12940, 1987.
- [3] G. Berrino, G. Corrado, G. Luongo, and B. Toro, "Ground deformation and gravity changes accompanying the 1982 pozzuoli uplift," *Bulletin volcanologique*, vol. 47, no. 2, pp. 187–200, 1984.
- [4] L. Karlstrom, J. Dufek, and M. Manga, "Magma chamber stability in arc and continental crust," *Journal of Volcanology and Geothermal Research*, vol. 190, no. 3-4, pp. 249–270, 2010.
- [5] C. Del Negro, G. Currenti, and D. Scandura, "Temperature-dependent viscoelastic modeling of ground deformation: Application to etna volcano during the 1993–1997 inflation period," *Physics of the Earth and Planetary Interiors*, vol. 172, no. 3-4, pp. 299–309, 2009.

- [6] M. Head, J. Hickey, J. Gottsmann, and N. Fournier, "The influence of viscoelastic crustal rheologies on volcanic ground deformation: Insights from models of pressure and volume change," *Journal of Geophysical Research: Solid Earth*, vol. 124, no. 8, pp. 8127–8146, 2019.
- [7] G. Currenti and C. A. Williams, "Numerical modeling of deformation and stress fields around a magma chamber: Constraints on failure conditions and rheology," *Physics of the Earth and Planetary Interiors*, vol. 226, pp. 14–27, 2014.
- [8] P. Segall, "Repressurization following eruption from a magma chamber with a viscoelastic aureole," *Journal of Geophysical Research: Solid Earth*, vol. 121, no. 12, pp. 8501–8522, 2016.
- [9] M. Bonafede, M. Dragoni, and F. Quarenì, "Displacement and stress fields produced by a centre of dilation and by a pressure source in a viscoelastic half-space: application to the study of ground deformation and seismic activity at campi flegrei, italy," *Geophysical Journal International*, vol. 87, no. 2, pp. 455–485, 1986.
- [10] Y. Zhan and P. Gregg, "How accurately can we model magma reservoir failure with uncertainties in host rock rheology?" *Journal of Geophysical Research: Solid Earth*, vol. 124, no. 8, pp. 8030–8042, 2019.
- [11] R. R. Bakker, M. Frehner, and M. Lupi, "How temperature-dependent elasticity alters host rock/magmatic reservoir models: A case study on the effects of ice-cap unloading on shallow volcanic systems," *Earth and Planetary Science Letters*, vol. 456, pp. 16–25, 2016.
- [12] J. Schöberl, "Netgen an advancing front 2d/3d-mesh generator based on abstract rules," *Computing and visualization in science*, vol. 1, no. 1, pp. 41–52, 1997.
- [13] J. Schöberl et al., "Netgen/ngsolve," 2017.
- [14] J. Schöberl, "C++ 11 implementation of finite elements in ngsolve," *Institute for Analysis and Scientific Computing, Vienna University of Technology*, vol. 30, 2014.
- [15] P. J. Roache, *Verification and validation in computational science and engineering*. Hermosa Albuquerque, NM, 1998, vol. 895.
- [16] P. Segall, *Earthquake and volcano deformation*. Princeton University Press, 2010.
- [17] S. Larsson and V. Thomée, *Partial differential equations with numerical methods*. Springer Science & Business Media, 2008, vol. 45.
- [18] J. Golden and G. Graham, *Boundary Value Problems in Linear Viscoelasticity*. Springer-Verlag, 1988. [Online]. Available: <https://books.google.com/books?id=zQ2oAAAAIAAJ>
- [19] K. L. Allison and E. M. Dunham, "Earthquake cycle simulations with rate-and-state friction and power-law viscoelasticity," *Tectonophysics*, vol. 733, pp. 232–256, 2018.